

# 3D tumor localization through real-time volumetric x-ray imaging for lung cancer radiotherapy

Ruijiang Li, John H. Lewis, Xun Jia, Xuejun Gu, Michael Folkerts, Chunhua Men, William Y. Song, and Steve B. Jiang<sup>a</sup>

*Center for Advanced Radiotherapy Technologies and Department of Radiation Oncology, University of California San Diego, La Jolla, CA 92037*

## Abstract

**Purpose:** To evaluate an algorithm for real-time 3D tumor localization from a single x-ray projection image for lung cancer radiotherapy.

**Methods:** Recently we have developed an algorithm for reconstructing volumetric images and extracting 3D tumor motion information from a single x-ray projection (Li *et al* 2010 *Med Phys* **37** 2822-6). We have demonstrated its feasibility using a digital respiratory phantom with regular breathing patterns. In this work, we present a detailed description and a comprehensive evaluation of the improved algorithm. The algorithm was improved by incorporating respiratory motion prediction. The accuracy and efficiency of using this algorithm for 3D tumor localization were then evaluated on 1) a digital respiratory phantom, 2) a physical respiratory phantom, and 3) five lung cancer patients. These evaluation cases include both regular and irregular breathing patterns that are different from the training dataset.

**Results:** For the digital respiratory phantom with regular and irregular breathing, the average 3D tumor localization error is less than 1 mm which does not seem to be affected by amplitude change, period change, or baseline shift. On an NVIDIA Tesla C1060 GPU card, the average computation time for 3D tumor localization from each projection ranges between 0.19 and 0.26 seconds, for both regular and irregular breathing, which is about a 10% improvement over previously reported results. For the physical respiratory phantom, an average tumor localization error below 1 mm was achieved with an average computation time of 0.13 and 0.16 seconds on the same GPU card, for regular and irregular breathing, respectively. For the five lung cancer patients, the average tumor localization error is below 2 mm in both the axial and tangential directions. The average computation time on the same GPU card ranges between 0.26 and 0.34 seconds.

**Conclusions:** Through a comprehensive evaluation of our algorithm, we have established its accuracy in 3D tumor localization to be on the order of 1 mm on average and 2 mm at 95 percentile for both digital and physical phantoms, and within 2 mm on average and 4 mm at 95 percentile for lung cancer patients. The results also indicate that the accuracy is not affected by the breathing pattern, be it regular or irregular. High computational efficiency can be achieved on GPU, requiring 0.1 - 0.3 s for each x-ray projection.

Key words: image reconstruction, tumor localization, GPU, lung cancer radiotherapy

## 46 I. INTRODUCTION

47

48 In modern lung cancer radiotherapy, it is important to have a precise knowledge of real-time lung  
49 tumor position during the treatment delivery<sup>1</sup>. Lung tumor localization methods can be broadly  
50 categorized as direct tumor localization, localization via breathing surrogates, and localization of  
51 implanted markers. Localization based on implanted markers has been shown to be highly  
52 accurate<sup>2</sup>. The major drawback is the invasive procedure of marker implantation and the  
53 associated risk of pneumothorax<sup>3</sup>. Surrogate-based localization sometimes involves no additional  
54 radiation dose to the patient (*e.g.*, optical localization) but suffers from the varying relationship  
55 between tumor motion and surrogates both intra- and inter- fractionally<sup>4, 5</sup>. Current radiotherapy  
56 treatment machines are usually equipped with an on-board imaging system, which consists of one  
57 kV x-ray source and one flat panel imager. Lung tumors may thus be tracked directly without  
58 implanted markers in fluoroscopic images acquired by the on-board imaging system<sup>6-9</sup>.  
59 Drawbacks of existing direct localization techniques include: 1) they work well mainly for  
60 images acquired from the anterior-posterior (AP) direction and the tumors with well-defined  
61 boundaries; 2) they usually require the training fluoroscopic data acquired and labeled prior to  
62 treatment; 3) the third dimension of tumor motion perpendicular to the x-ray imager cannot be  
63 resolved.

64

65 These drawbacks may be overcome if a good lung motion model is used for direct tumor  
66 localization. Zeng *et al.* used a generic B-spline lung motion model<sup>10</sup> to estimate 3D respiratory  
67 motion from cone beam projections. However, because of the large number of parameters in the  
68 model, multiple projections (over a 180° gantry rotation) are required to obtain a reasonable  
69 estimate for the model parameters. The estimation is thus retrospective and the computation  
70 takes quite a long time (several hours on MATLAB). It is clearly not sufficient for use in real-  
71 time tumor localization, which has to be done on a sub-second scale. Zhang *et al.* developed a  
72 lung motion model based on principal component analysis (PCA), which can efficiently represent  
73 the lung motion with only a few eigenvectors and PCA coefficients<sup>11</sup>. The PCA lung motion  
74 model has recently been shown to bear a close relationship with the physiological 5D lung motion  
75 model proposed by Low *et al.*<sup>12</sup> on a theoretical basis<sup>13</sup>. It is the implicit regularization and high  
76 efficiency of the PCA lung motion model that allows one to derive the dynamic lung motion in a  
77 reasonably accurate and efficient way, given a very limited amount of information, *e.g.*, a single  
78 x-ray projection.

79

80 In our previous work<sup>14</sup>, we have described an algorithm based on the PCA lung motion model and  
81 demonstrated the feasibility of reconstructing volumetric images and extracting 3D tumor motion  
82 information in real time from a single x-ray projection using a digital respiratory phantom with  
83 regular breathing patterns. In this paper, we will present a detailed description of our improved  
84 algorithm and extend the scope of our previous work. In particular, the new contributions of this  
85 work relative to our previous work<sup>14</sup> are: 1) a comprehensive evaluation of the algorithm for 3D  
86 tumor localization using digital and physical respiratory phantoms as well as lung cancer patients  
87 with both regular and irregular breathing patterns, which are different from those in the training  
88 dataset; 2) improved efficiency obtained from better initialization of the PCA coefficients using  
89 prediction methods.

90

## 91 II. METHODS AND MATERIALS

92

93 For completeness, we first briefly describe the methods for volumetric image reconstruction,  
94 which were first presented by Li *et al.*<sup>14</sup>. We also discuss ways to further speed up the  
95 optimization. Then, we test our algorithm using cone beam CT (CBCT) projections in three  
96 different scenarios, namely, a digital respiratory phantom, a physical respiratory phantom, and  
97 five lung cancer patients. We reconstructed the volumetric image and derived the 3D tumor

98 location corresponding to each CBCT projection. To quantify the accuracy of our algorithm for  
 99 tumor localization, we used the average absolute error (denoted as  $\bar{e}$ ) as well as the absolute error  
 100 at 95 percentile (denoted as  $e_{95}$ ).

## 101 102 **II.A. Methods**

103  
 104 Our method for volumetric image reconstruction and 3D tumor localization uses 4DCT from  
 105 treatment simulation as a priori knowledge. Deformable image registration is performed between  
 106 a reference phase and the other phases, resulting in a set of deformation vector fields (DVF).  
 107 This set of DVFs can be represented efficiently by a few eigenvectors and coefficients obtained  
 108 from PCA. By changing the PCA coefficients, we can generate a new DVF. A new volumetric  
 109 image can be obtained when the DVF is applied on the reference image. We then optimize the  
 110 PCA coefficients such that its computed projection image matches the measured one of the new  
 111 volumetric image. The 3D location of the tumor can be derived by applying the inverted DVF on  
 112 its position in the reference image.

113  
 114 In the PCA lung motion model<sup>11</sup>, the DVF relative to a reference image as a function of space and  
 115 time is approximated by a linear combination of the sample mean vector and a few eigenvectors  
 116 corresponding to the largest eigenvalues, *i.e.*,

$$117 \quad \mathbf{x}(t) \approx \bar{\mathbf{x}} + \sum_{k=1}^K \mathbf{u}_k w_k(t). \quad (1)$$

118 where  $\mathbf{x}(t)$  is the parameterized DVF as a function a space and time,  $\bar{\mathbf{x}}$  is the mean DVF with  
 119 respect to time;  $\mathbf{u}_k$  are the eigenvectors obtained from PCA and are functions of space; the  
 120 scalars  $w_k(t)$  are PCA coefficients and are functions of time. It is worth mentioning that the PCA  
 121 motion model is so flexible that it is capable of represent tumor motion which is beyond that of  
 122 the training set. For instance, if the PCA coefficients are allowed to change arbitrarily, then given  
 123 two eigenvectors, the tumor can move anywhere in a plane defined by the corresponding entries  
 124 in the eigenvectors, and thus hysteresis motion can be handled; given three eigenvectors, the  
 125 tumor can move anywhere in the space. The reason for this is that each voxel is associated with  
 126 three entries (corresponding to three canonical directions in space) in each and every eigenvector.  
 127 Therefore, each eigenvector defines a vector (or a direction) in space along which each voxel  
 128 moves; two eigenvectors span a plane; and three eigenvectors span the entire 3D space where the  
 129 tumor can move. This important feature enables the PCA motion model to capture a wide range  
 130 of tumor motion trajectories. In this study, we kept the first three PCA coefficients in the PCA  
 131 lung motion model. This is mainly motivated by the fact that three is the least number of PCA  
 132 coefficients that are capable of capturing a full 3D tumor motion trajectory. On the other hand,  
 133 using more PCA coefficients, although more flexible, could lead to the overfitting problem and is  
 134 not necessary.

135  
 136 After we have obtained a parameterized PCA lung motion model, we seek a set of optimal PCA  
 137 coefficients such that the projection of the reconstructed volumetric image corresponding to the  
 138 new DVF matches with the measured x-ray projection. Denote  $\mathbf{f}_0$  as the reference image,  $\mathbf{f}$  as  
 139 the reconstructed image,  $\mathbf{y}$  as the measured projection image, and  $\mathbf{P}$  as a projection matrix  
 140 which computes the projection image of  $\mathbf{f}$ . The cost function is:

$$141 \quad \min J(\mathbf{w}, a, b) = \left\| \mathbf{P} \cdot \mathbf{f}(\mathbf{x}, \mathbf{f}_0) - a \cdot \mathbf{y} - b \cdot \mathbf{1} \right\|_2^2 \quad (2)$$

$$142 \quad s.t. \quad \mathbf{x} = \bar{\mathbf{x}} + \mathbf{U} \cdot \mathbf{w}$$

143 where,  $\mathbf{U}$  is a matrix whose columns are the PCA eigenvectors and  $\mathbf{w}$  is a vector comprised of  
 144 the PCA coefficients to be optimized,  $\mathbf{x}$  is the parameterized DVF, and  $\|\cdot\|_p$  denotes the standard  
 vector  $l_p$ -norm. Because the computed and measured projection images may have different pixel

145 intensity levels, we assume there exists a linear relationship between them and introduce two  
 146 auxiliary parameters  $a$  and  $b$  to account for the differences. In the Appendix we describe in detail  
 147 the optimization of the cost function with respect to  $\mathbf{w}, a, b$ .

148

149 Selecting good initial conditions for the parameters may help speed up the convergence of the  
 150 algorithm. In our previous work<sup>14</sup>, we  
 151 initialized the PCA coefficients to those  
 152 obtained for the last projection. A better  
 153 approach is to consider the last few  
 154 projections and initialize the PCA  
 155 coefficients to their predicted values,  
 156 taking into account the respiratory  
 157 dynamics. This might become important  
 158 when the imaging frequency is low. There  
 159 is a vast amount of literature on respiratory  
 160 motion prediction models<sup>15-17</sup> that we can  
 161 use. In this paper, we used a simple linear  
 162 prediction model<sup>16</sup> which predicts the  
 163 current sample using a linear combination  
 164 of several previous samples, *i.e.*,

$$165 \quad w_{k0}(t) = \sum_{l=1}^L c_{kl} \cdot w_k^*(t-l) \quad (3)$$

166 where,  $w_{k0}(t)$  is the initial guess for the  $k$ -th  
 167 PCA coefficients for the current  
 168 projection;  $w_k^*(t-l)$  is the optimized  $k$ -th  
 169 PCA coefficients for previous  $l$ -th  
 170 projections. Note that each PCA coefficient  
 171 has a prediction model associated with it  
 172 since they have different dynamics.

173

174 In this paper, we utilize the training set  
 175 (*i.e.*, 4DCT) to build the prediction model  
 176 (alternatively, the first few breathing cycles  
 177 during the CBCT scan may be used to  
 178 build the prediction model). Because the  
 179 sampling rate for 4DCT and CBCT scan is  
 180 different (for instance, for a patient with a  
 181 4-sec breathing period, the sampling rate  
 182 for 4DCT is 2.5 Hz if 10 phases were  
 183 reconstructed; on the other hand, the  
 184 sampling rate for CBCT projections is  
 185 faster, usually on the order of 10 Hz for a  
 186 typical 1-min scan with around 600  
 187 projections), we first interpolated the PCA  
 188 coefficients from the training set and re-  
 189 sampled to have the same frequency as in  
 190 CBCT scan. Then the model fitting process  
 191 was done separately for each of the PCA  
 192 coefficients since they are assumed to be  
 193 independent in the PCA motion model.  
 194 Here, we would like to point out that the

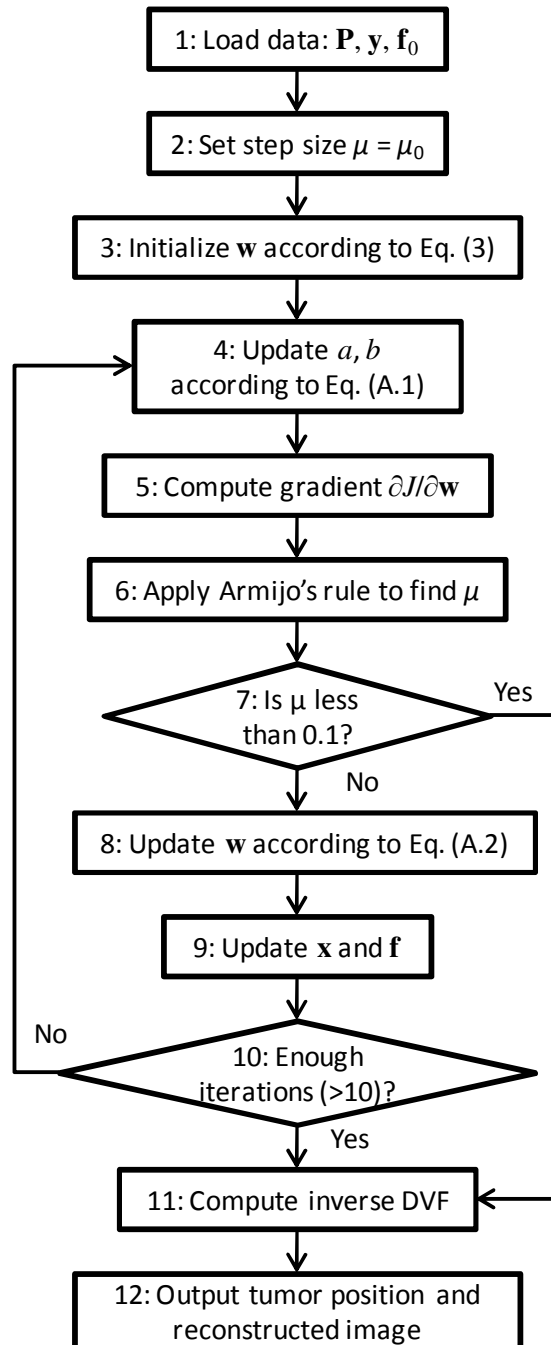


**Fig. 1.** The flow chart of the proposed algorithm for volumetric image reconstruction and tumor localization based on a single x-ray projection. For the meaning of step size and gradient as well as expressions of Eq. (A.1), Eq. (A.2), refer to the Appendix.

195 primary goal of the prediction model is to obtain a "good" initial guess for the PCA coefficients,  
196 so that the efficiency of the algorithm may be improved. For this purpose, the linear model used  
197 here seems sufficient.

198  
199 In order to get the current tumor position, we note that the DVF found by Eq. (2) is a pull-back  
200 DVF, which is defined on the coordinate of the new image and tells how each voxel in the new  
201 image moves. It cannot be used directly to calculate the tumor position in the new image unless  
202 the DVF is rigid everywhere. To get the correct tumor position, we need its inverse, *i.e.*, the push-  
203 forward DVF, which is defined on the coordinate of the reference image and tells how each voxel  
204 in the reference image moves. In this work, we adopted an efficient fixed-point algorithm for  
205 deformation inversion, which has been shown to be about 10 times faster and yet 10 times more  
206 accurate than conventional gradient-based iterative algorithms<sup>18</sup>. Since we are primarily  
207 concerned with the tumor motion, it is not necessary to apply the deformation inversion  
208 procedure on the entire image. Instead, it is applied on only one voxel, which corresponds to the  
209 tumor center of volume in the reference image. Finally, we summarize our algorithm in a flow  
210 chart, as shown in Fig. 1.

211  
212 To achieve real-time efficiency, we have implemented our algorithm on graphic processing units  
213 (GPUs). For this work, we used compute unified device architecture (CUDA) as the  
214 programming environment and an NVIDIA Tesla C1060 GPU card.

215  
216 For evaluation purposes, we used the end of exhale (EOE) phase in 4DCT as the reference image  
217 and performed deformable image registration (DIR) between the EOE phase and all other phases.  
218 The DIR algorithm used here is a fast demons algorithm implemented on GPU<sup>19</sup>. Then PCA was  
219 performed on the nine DVFs from DIR and three PCA coefficients and eigenvectors were kept in  
220 the PCA lung motion model (except for the physical phantom, where the motion is along the  
221 longitudinal axis so that only one PCA coefficient is necessary). For the prediction model in Eq.  
222 (3), we selected  $L = 2$  in all the cases.

## 223 224 **II.B. Digital respiratory phantom**

225  
226 The algorithm was first tested using a non-uniform rational B-spline (NURBS) based cardiac-  
227 torso (NCAT) phantom<sup>20</sup>. In this work, we considered three fundamental breathing parameters:  
228 namely amplitude, period, and baseline shift relative to the training dataset. In the case of regular  
229 breathing, we first used the same breathing parameters as those in the training set and generated  
230 testing volumetric images. We then systematically changed the breathing pattern such that each  
231 time, only one of the three parameters was changed while the other two were kept the same as  
232 those in the training set. In doing so, we can independently evaluate the effects of each of the  
233 three breathing parameters. The different breathing parameters considered in this work are:  
234 amplitude (diaphragm motion: 1 cm and 3 cm), period (3 s and 5 s), and baseline shift (1 cm  
235 toward the EOE phase and EOI phase). In the case of irregular breathing, we used a scaled  
236 version of the breathing signal of a real patient acquired by the Real-time Position Management  
237 (RPM) system (Varian Medical Systems, Palo Alto, CA, USA). The dynamic NCAT phantom  
238 motion can be generated by specifying the diaphragm SI motion. In this case, the scaled RPM  
239 signal was then used as a substitute for the diaphragm SI motion of the NCAT phantom. The  
240 breathing signal from RPM has a varying breathing amplitude (between 1.0 and 2.5 cm), period  
241 (between 3.5 and 6.2 s), and a baseline shift of about 1 cm.

242  
243 After we obtained the dynamic NCAT phantom, we then simulated 360 cone beam projections  
244 using the Siddon's algorithm<sup>21</sup> from angles that are uniformly distributed over one full gantry  
245 rotation (*i.e.*, the angular spacing between consecutive projections is 1°). For instance, the cone  
246 beam projection at angle 180° corresponds to the dynamic phantom at 30 sec, and the projection

247 at angle  $360^\circ$  corresponds to the dynamic phantom at 60 sec, and so on. Since the gantry rotation  
248 lasts 60 seconds, the sampling rate of the cone beam projections is 6 Hz. We did not add any  
249 quantum noise in the simulated x-ray projections for the digital phantom cases. However,  
250 intrinsic quantum noise is present in all physical phantom and patient projections and no noise  
251 reduction was attempted on those images. The imager has a physical size of  $40 \times 30 \text{ cm}^2$ . For  
252 efficiency considerations, we down-sampled every measured projection image to a resolution of  
253  $200 \times 150$  (pixel size:  $2 \times 2 \text{ mm}^2$ ).

### 254 255 **II.C. Physical respiratory phantom**

256  
257 The algorithm was also tested on a simple physical respiratory phantom. The phantom consisted  
258 of a cork block resting on a platform that can be programmed to undergo translational motion in  
259 one dimension. This platform was used to simulate the SI respiratory motion of a lung tumor.  
260 Inside the cork block were embedded several tissue-like objects including a 2.5 cm water balloon  
261 which was used as the target for localization. More detailed descriptions of the phantom can be  
262 found in Lewis *et al.*<sup>9</sup>.

263  
264 4DCT of the physical phantom was acquired using a GE four-slice LightSpeed CT scanner (GE  
265 Medical Systems, Milwaukee, WI, USA) and the RPM system. During the 4DCT scan, the  
266 physical phantom moved according to a sinusoidal function along the SI direction, with a peak-  
267 to-peak amplitude of 1.0 cm. In order to calculate the correct projection matrix and image for the  
268 algorithm, the CT image corresponding to the EOE phase in 4DCT was re-sampled in space to  
269 have the same spatial resolution as CBCT and then rigidly registered to the CBCT. Since only  
270 rigid registration was performed at this stage, in reality, paired kV radiographs may also be used  
271 to achieve this task during patient setup. Cone-beam projections were acquired using Varian On-  
272 Board Imager 1.4 in full-fan mode with 100 kVp, 80 mA and 25 ms exposure time. The x-ray  
273 imager has a physical size of  $40 \times 30 \text{ cm}^2$  and each projection image has a resolution of  $1024 \times 768$ .

274  
275 For testing purposes, we performed two CBCT scans for the physical phantom: one with regular  
276 breathing, and the other with irregular breathing. For the case of regular breathing, the phantom  
277 moved according to a sinusoidal function along the SI direction, with an increased peak-to-peak  
278 amplitude of 1.5 cm. For the case of irregular breathing, the phantom moved according to the  
279 same RPM signal used for the digital phantom as described before, with the peak-to-peak  
280 amplitude scaled to 1.5 cm. In both cases, 359 bone beam x-ray projections were acquired over an  
281 arc of around  $200^\circ$  with a frequency of about 10.7 Hz. The CBCT scans for the physical phantom  
282 lasted for about 36 s, so only the first 36 s of the RPM signal was used during the scan. Since the  
283 motion of the physical phantom during the CBCT scan is known, it was used as the ground truth  
284 to evaluate the accuracy of target localization.

285  
286 The following preprocessing was performed on each of the cone beam x-ray projections. First,  
287 due to the presence of the full-fan bow-tie filter near the x-ray source, a systematic bias will be  
288 introduced in the linear relations between the image intensities of the simulated and measured  
289 projections. So an in-air x-ray projection with exactly the same imaging protocol was acquired in  
290 order to correct for the systematic bias. This was done by dividing each pixel intensity value of  
291 the projection images acquired for the physical phantom by those in the in-air projection image.  
292 Each corrected projection image was then down-sampled by a factor of 4, resulting in a resolution  
293 of  $256 \times 192$  (pixel size:  $1.56 \times 1.56 \text{ mm}^2$ ). The rationale and effect of downsampling will be  
294 discussed later in the paper.

## 299 **II.D. Patient data**

300

301 Finally, the algorithm was evaluated with five patient data sets. Both 4DCT and CBCT were  
302 acquired using the same imaging systems as for the physical phantom. The cone beam projections  
303 were taken with the imaging system in half-fan mode with 110 kVp, 20 mA and 20 ms exposure  
304 time. Similarly to the physical phantom, the CT at the EOE phase was re-sampled in space and  
305 then rigidly registered to the CBCT according to the bones. The same preprocessing on each of  
306 the raw cone beam projections of the patient was used as for the physical phantom, namely,  
307 cutoff, downsampling, and a logarithm transform, except for the bow-tie filter correction, which  
308 was based on the half-fan mode. For patient 2, however, since the computed projections of the  
309 4DCT did not have sufficient longitudinal coverage compared with the cone beam projections, an  
310 additional 3 cm was cut off from the raw cone beam projections in both superior and inferior  
311 directions.

312

313 For all patients in this study, there were no implanted fiducial makers and real-time 3D location  
314 of the tumor was not available to evaluate our algorithm. Instead, we projected the estimated 3D  
315 tumor location onto the 2D imager and compared with that manually defined by a clinician. The  
316 patients chosen for this study had tumors that were visible to the clinician in some of the cone  
317 beam projections. From the clinician-defined contour, the tumor centroid position was calculated  
318 for each projection and used as the ground truth to evaluate the algorithm. We calculated the  
319 tumor localization error along the axial and tangential directions, both scaled back to the mean  
320 tumor position. The axial direction is defined to be along the axis of rotation on the imager and  
321 the tangential direction is perpendicular to the axis of rotation on the imager. For a tumor located  
322 near the isocenter, the tumor motion along the axial direction on the imager is roughly a scaled  
323 version of its SI motion in the patient coordinate system. On the other hand, the tumor motion  
324 along the tangential direction is a mixture of its AP and LR motions depending on the imaging  
325 angle. In some special cases, the tumor motion along the tangential direction can be roughly a  
326 scaled version of either the AP motion (for imaging angles near LR or RL) or LR motion (for  
327 imaging angles near AP or PA). Since the tumor is hard to see in some of the projections, the  
328 uncertainty in the definition of ground truth can be large, and may depend on the angle at which a  
329 projection is taken. A rough estimate of the uncertainty in the ground truth based on comparing  
330 contours drawn from two observers suggests that the error in centroid position is about 1-2 mm  
331 on average.

332

333 For each patient, approximately 650 projections were acquired over a full gantry rotation with a  
334 frequency of about 10.7 Hz. However, since the cone beam scans were performed in the half-fan  
335 mode (with the imager shifted about 14.8 cm laterally), and isocenter of the scan was not placed  
336 at the tumor, the tumor is only visible in a subset of these projections. For each patient, the tumor  
337 was marked by the clinician in the largest continuous set of projections in which the tumor was  
338 visible. For the five patients, the number of cone beam projections used for this study ranged  
339 between 70 and 281, corresponding to angles of 39° and 155°, respectively.

340

## 341 **II.E. Summary of testing cases**

342

343 Table 1 summarizes all the testing cases in this work, including 8 digital phantom cases, 2  
344 physical phantom cases, and 5 lung cancer patient cases. The table lists the relevant breathing  
345 parameters that were used during the CBCT scan for tumor localization purposes. It also includes  
346 information on the tumor size, location, as well as motion characteristics as measured in 4DCT  
347 for the 5 lung cancer patients.

348

349 **Table 1.** Summary of all testing cases. For the digital phantom, the breathing parameters in the training  
 350 dataset are: 2 cm amplitude, 4 s period, and 0 cm baseline shift; for cases 2 through 7, all breathing  
 351 parameters are the same as in training dataset except the one indicated in the table. All parameters for lung  
 352 cancer patients were measured in 4DCT.

Case #	Category	Relevant Parameters
1	Digital phantom 1	Same as training
2	Digital phantom 2	Amplitude changed to 1 cm
3	Digital phantom 3	Amplitude changed to 3 cm
4	Digital phantom 4	Period changed to 3 s
5	Digital phantom 5	Period changed to 5 s
6	Digital phantom 6	Baseline shift changed to 1 cm toward the EOE phase
7	Digital phantom 7	Baseline shift changed to 1 cm toward the EOI phase
8	Digital phantom 8	Breathing changed to irregular patient breathing
9	Physical phantom 1	Amplitude changed to 1.5 cm (training: 1 cm)
10	Physical phantom 2	Breathing changed to irregular patient breathing
11	Lung cancer patient 1	2.7 cm <sup>3</sup> tumor at right lower lobe; 20 mm tumor motion
12	Lung cancer patient 2	18.3 cm <sup>3</sup> tumor at left lower lobe; 17 mm tumor motion
13	Lung cancer patient 3	8.1 cm <sup>3</sup> tumor at left upper lobe; 5 mm tumor motion
14	Lung cancer patient 4	3.3 cm <sup>3</sup> tumor at right lower lobe; 11 mm tumor motion
15	Lung cancer patient 5	10.2 cm <sup>3</sup> tumor at left lower lobe; 12 mm tumor motion

353  
354

### 355 III. Results

356  
357 **Table 2.** Summary of localization accuracy and computational time for all testing cases. For the description  
 358 of each case, refer to Table 1. For Cases 1 through 10 (digital and physical phantoms), the localization  
 359 errors were computed in 3D; for Cases 11 through 15 (lung cancer patients), the localization errors were  
 360 computed on the axial and tangential directions with respect to the imager.

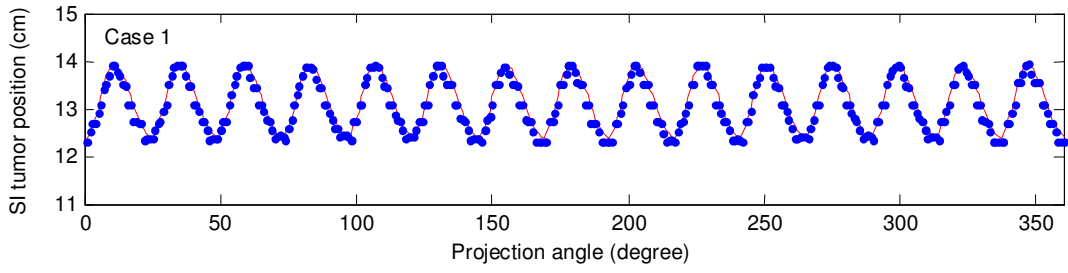
Case #	$\bar{e}$ (mm)		$e_{95}$ (mm)		Time (s)
1	0.8		1.8		0.20 ± 0.05
2	0.7		1.7		0.19 ± 0.05
3	0.8		1.8		0.22 ± 0.06
4	0.8		1.8		0.20 ± 0.05
5	0.8		1.8		0.20 ± 0.05
6	0.8		1.6		0.24 ± 0.05
7	0.8		1.8		0.24 ± 0.05
8	0.8		1.6		0.26 ± 0.06
9	0.8		2.2		0.13 ± 0.04
10	0.8		2.4		0.16 ± 0.05
–	Axial	Tangential	Axial	Tangential	–
11	1.5	1.8	3.1	3.6	0.29 ± 0.07
12	1.9	1.8	3.7	3.8	0.31 ± 0.12
13	0.4	0.9	1.0	2.5	0.26 ± 0.04
14	0.9	1.0	2.1	2.4	0.34 ± 0.09
15	1.1	0.4	2.7	1.2	0.33 ± 0.11

361  
362  
363

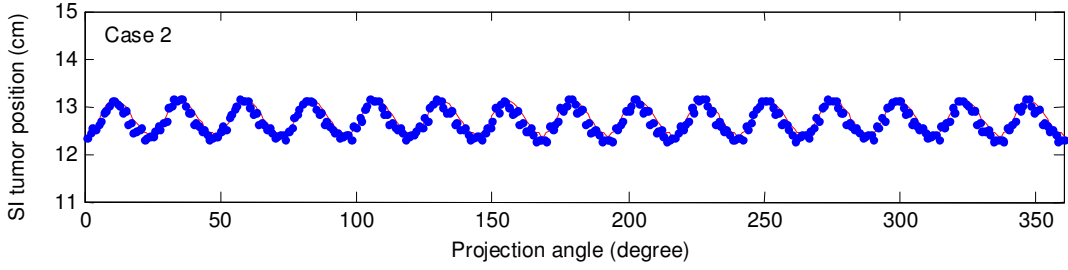
#### 364 III.A. Results for the digital respiratory phantom

365 Figure 2 shows the SI tumor position estimated by our algorithm as well as the ground truth for  
 366 the digital respiratory phantom for Cases 1 through 8. The numerical results for localization  
 367 accuracy and computational time are summarized in Table 2. The average 3D tumor localization  
 368 error for regular breathing with different breathing parameters is less than 1 mm, which does not  
 369 seem to be affected by amplitude change, period change, or baseline shift. The same holds true  
 for irregular breathing.

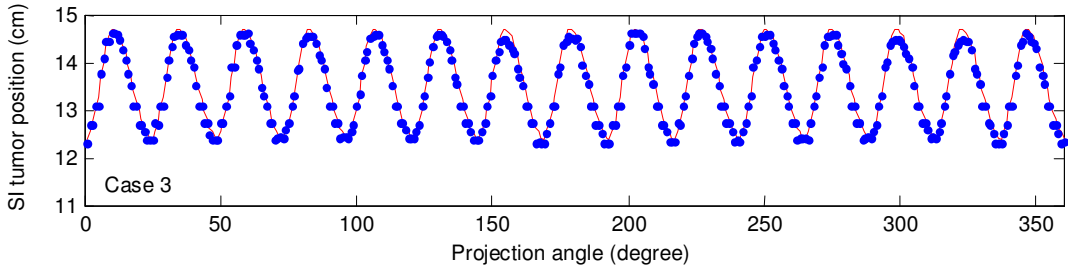
370



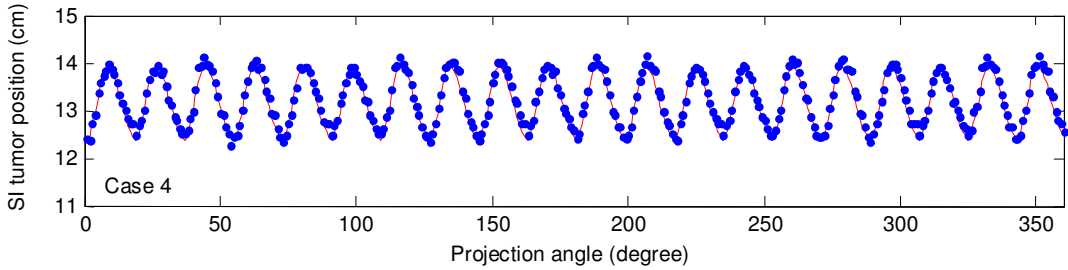
371



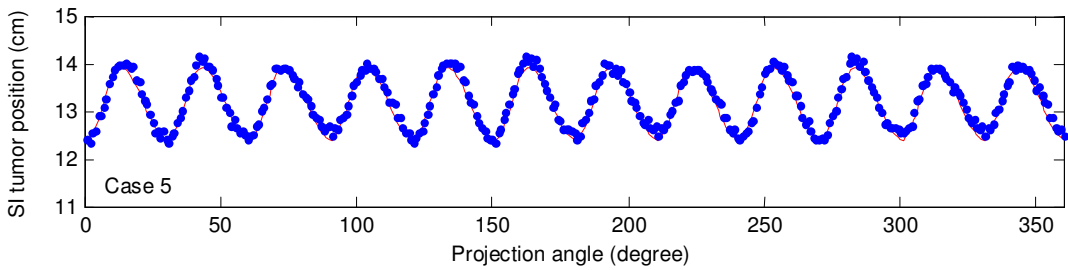
372



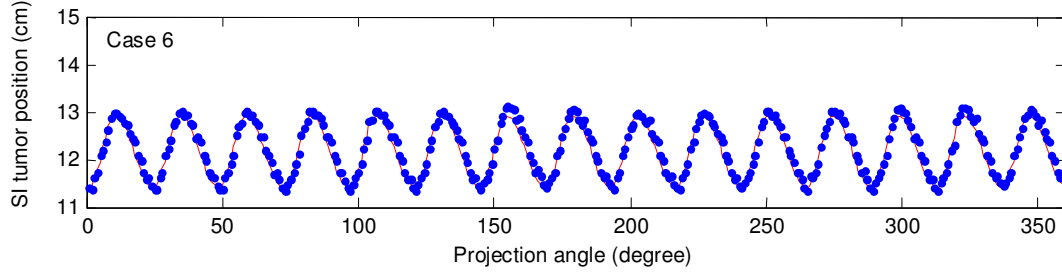
373



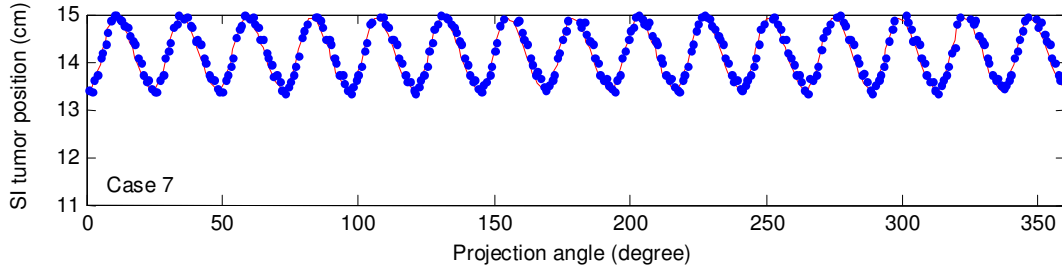
374



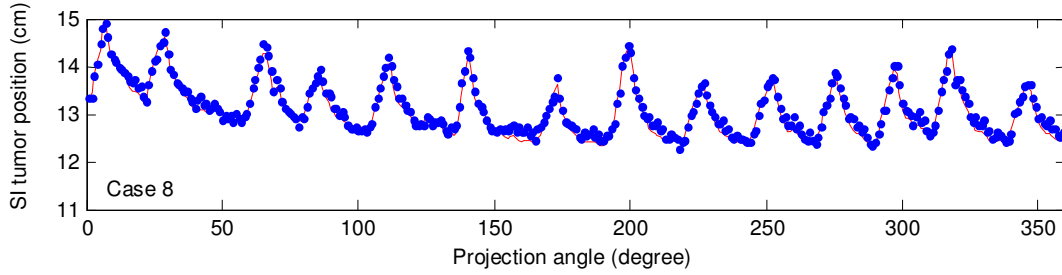
375



376



377



378

379

**Fig. 2.** SI tumor position estimated by our algorithm (black circles) and the ground truth (solid line) for the digital phantom (Cases 1 through 8).

380

381

382

From the re-sampled PCA coefficients in the training set, the prediction models were estimated as:

383

$$\begin{aligned}
 w_{1,0}(t) &= 1.90w_1^*(t-1) - 0.98w_1^*(t-2) \\
 w_{2,0}(t) &= 1.51w_2^*(t-1) - 0.84w_2^*(t-2) \\
 w_{3,0}(t) &= 0.97w_3^*(t-1) - 0.84w_3^*(t-2)
 \end{aligned} \tag{4}$$

384

385

386

387

388

389

390

391

392

393

By initializing the PCA coefficients to their predicted values using the above equations, the average computation time for both regular and irregular breathing ranges between 0.19 and 0.26 seconds using an NVIDIA Tesla C1060 GPU card. Particularly, the average computation time is 0.22 seconds in the case of regular breathing with a breathing amplitude of 3 cm. This is about 10% less than that previously reported<sup>14</sup> using the PCA coefficients from the previous projection. In the case of irregular breathing, the average computation time is  $0.26 \pm 0.06$  seconds. The slight increase in computation time for irregular breathing was mainly due to a decreased accuracy of the prediction model used for parameter initialization.

394

### III.B. Results for the physical respiratory phantom

395

396

397

398

399

Figure 3 shows the estimated and ground truth tumor position in the SI direction for both regular and irregular breathing. The numerical results for localization accuracy and computational time are summarized in Table 2 (Cases 9 and 10). The average 3D tumor localization error for both regular and irregular breathing is less than 1 mm.

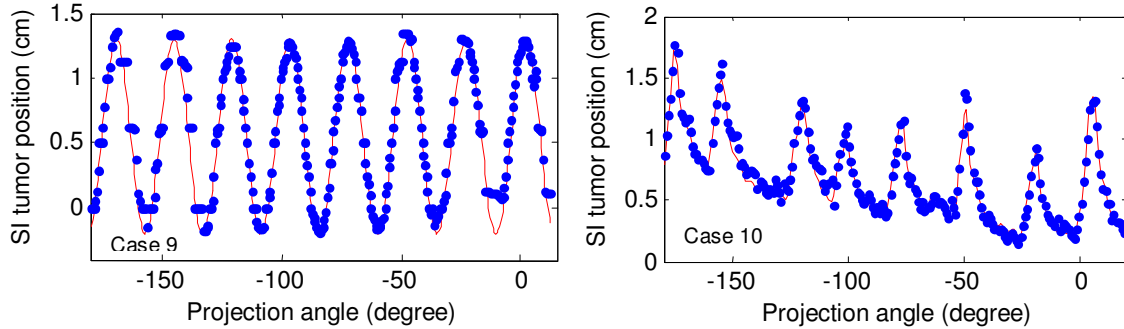
400

401 Since only one PCA coefficient was used for the physical phantom, the prediction model was  
402 estimated as:

$$w_{1,0}(t) = 1.96w_1^*(t-1) - 0.99w_1^*(t-2) \quad (5)$$

403

404 When PCA coefficients were initialized to their predicted values, the average computation time  
405 on GPU is 0.13 seconds and 0.16 seconds, for regular and irregular breathing, respectively. The  
406 reduced computation time compared with the NCAT phantom is mainly due to the less number of  
407 PCA coefficients used for the physical phantom.  
408



409

410 **Fig. 3.** SI tumor position estimated by our algorithm (black circles) and the ground truth (solid line) for the  
411 physical phantom (Cases 9 and 10). Left: regular breathing; Right: irregular breathing.

412

### 413 III.C Results for the patient data

414

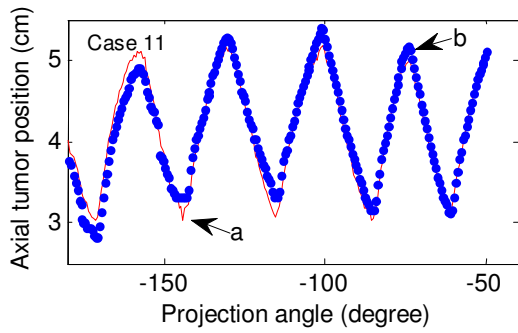
415 Results for the five lung cancer patients are shown in Fig. 4, where the tumor positions on the  
416 axial and tangential directions are shown separately. All five patients had somewhat irregular  
417 breathing during the CBCT scans especially for patient 2 (Case 12) and the last breathing cycle of  
418 patient 4 (Case 14). Again, the numerical results for localization accuracy and computational time  
419 are summarized in Table 2 (Cases 11 through 15). For all five patients, the average 3D tumor  
420 localization error is less than 2 mm and the absolute error at 95 percentile is less than 4 mm on  
421 both axial and tangential directions. When PCA coefficients were initialized to their predicted  
422 values, the average computation time on GPU is between 0.26 seconds and 0.34 seconds for the  
423 five patients.

424

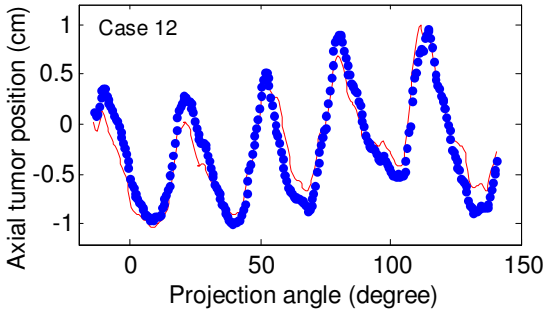
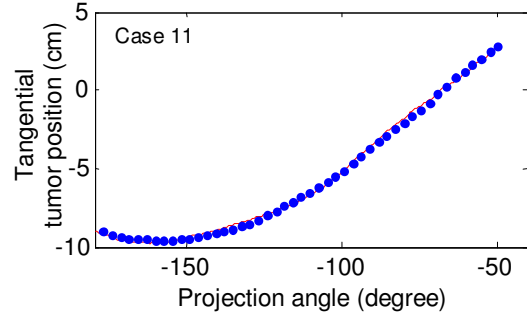
425 Figure 5 shows the image reconstruction and tumor localization results for patient 1 at an EOE  
426 phase and an EOI phase (indicated in Figure 4, Case 11), as well as the corresponding cone beam  
427 x-ray projections. Although it is hard to see the tumor on the projections, it is clearly visible in the  
428 coronal and sagittal slices of the reconstructed images.

429

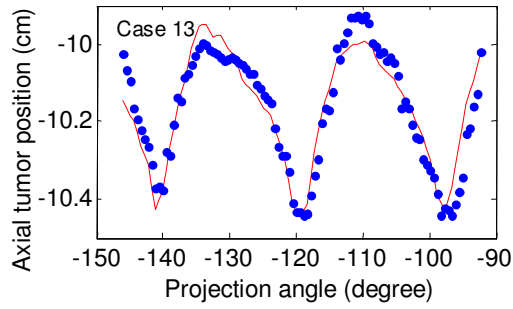
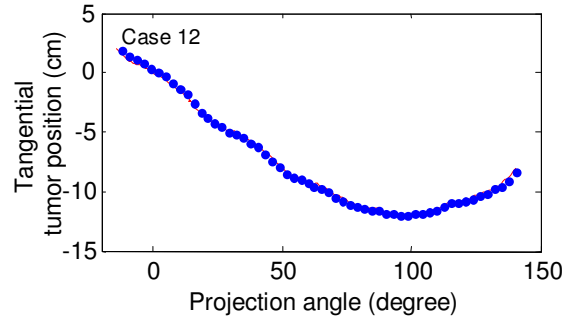
430



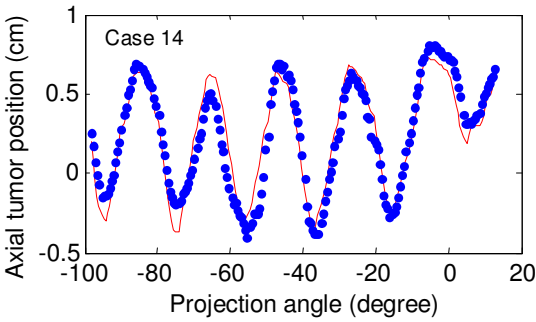
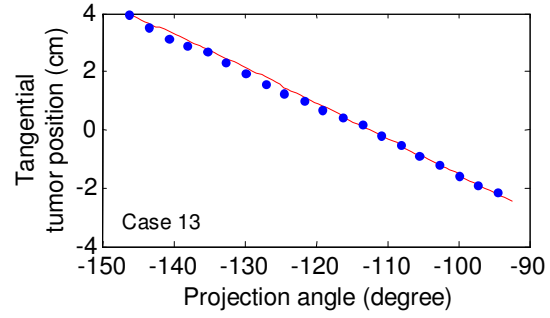
431



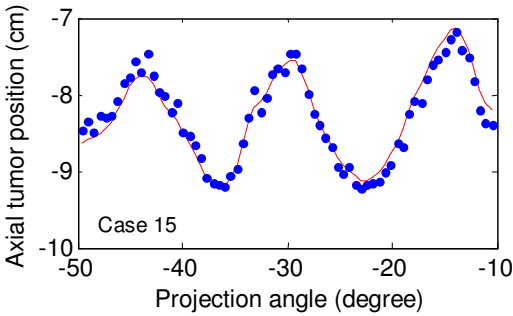
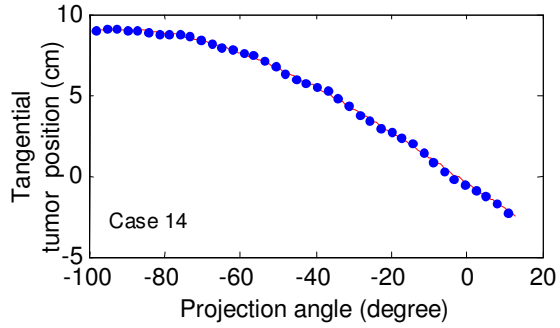
432



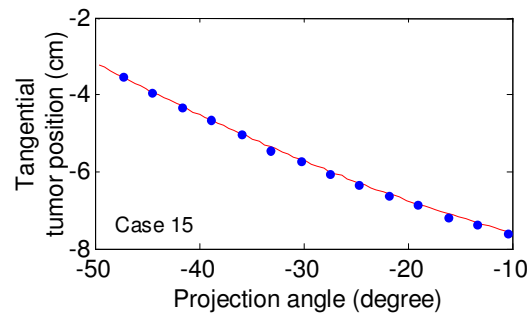
433



434



435



436

437

438

**Fig. 4.** Tumor positions estimated by our algorithm (black circles) and the ground truth (solid line) for five lung cancer patients (Cases 11 to 15). Left: axial tumor position; Right: tangential tumor position. The two

439 arrows ("a" and "b") in the left plot of patient 1 (Case 11) indicate the two angles where the image  
440 reconstructions results are shown in Fig. 5.  
441

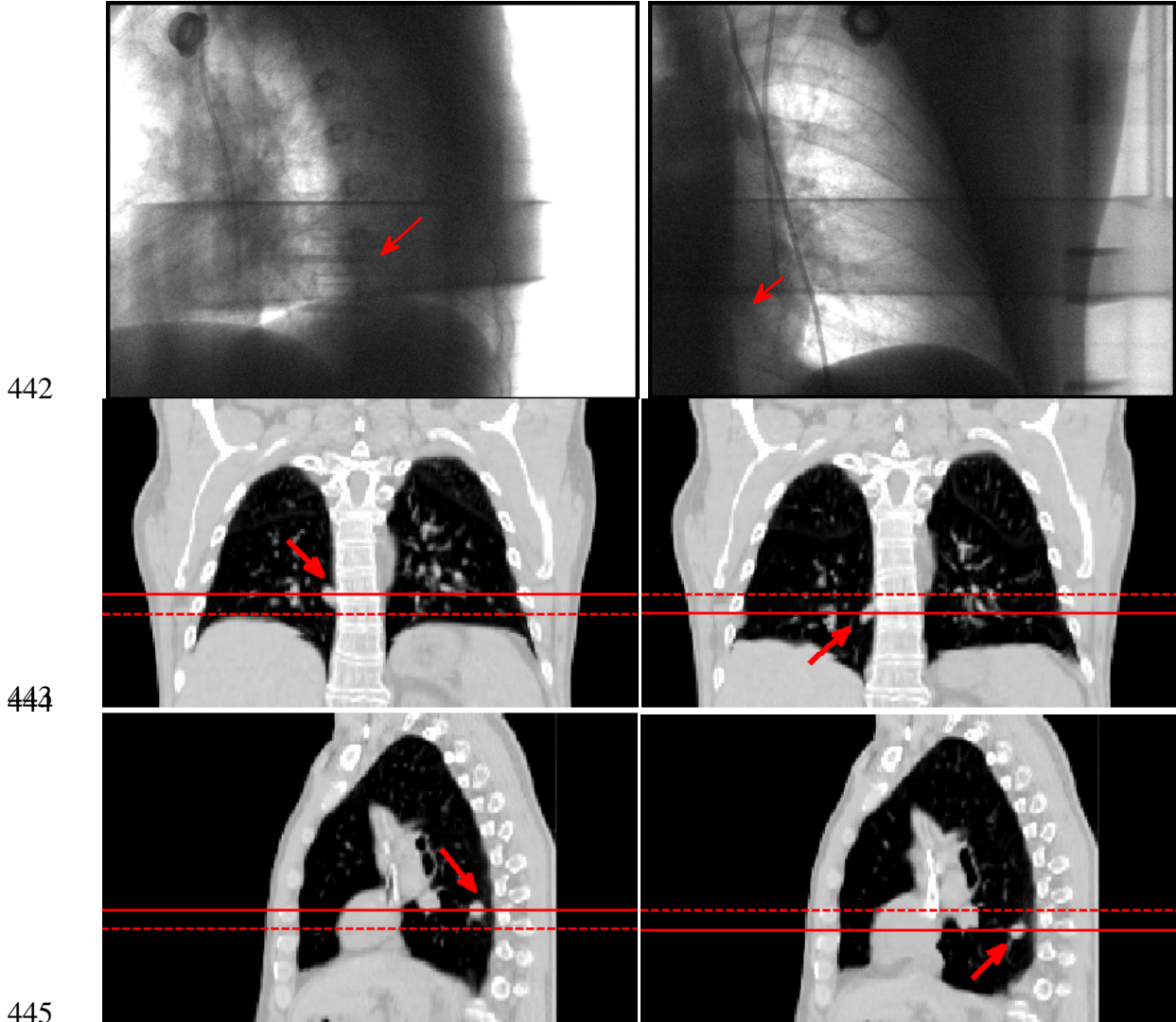
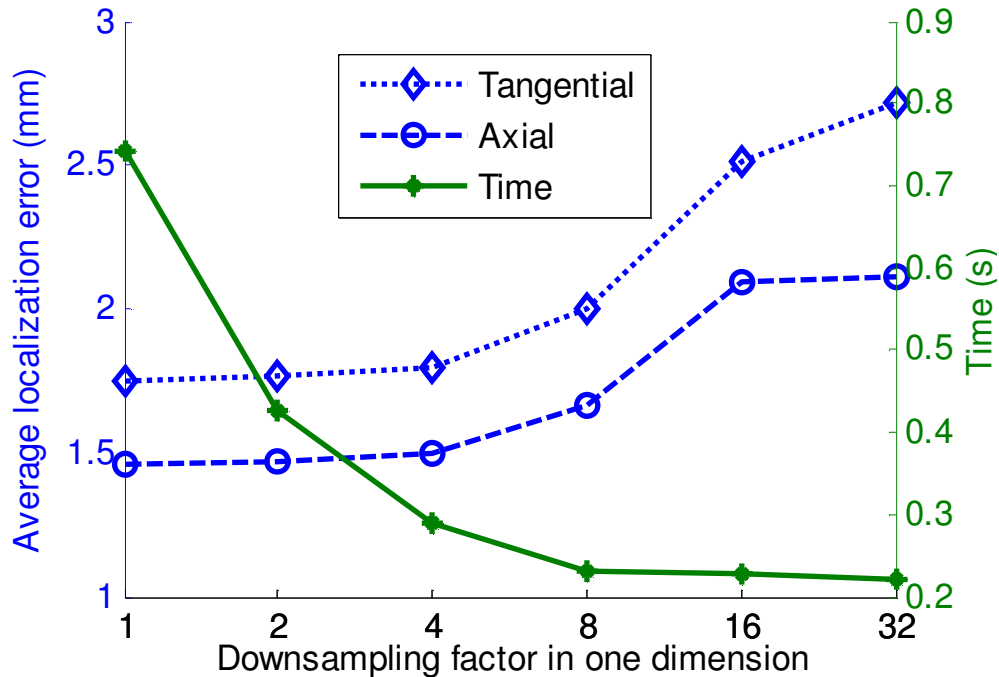


**Fig. 5.** Image reconstruction and tumor localization results for patient 1. Left column: raw cone beam projection (*top*) and the corresponding coronal and sagittal views of the reconstructed image at angle  $-146.5^\circ$  at an EOE phase (arrow "a" in Fig. 4). Right column: same as left column, except for angle  $-74.5^\circ$  at an EOI phase (arrow "b" in Fig. 4). Red arrow indicates where the tumor was. The solid line represents the estimated tumor SI position at the current phase; the dashed line represents the estimated tumor SI position at the other phase.

453 There is a tradeoff between the localization accuracy and computational time, which is dependent  
454 on the resolution of the projection image. Intuitively, as the image resolution is increased, the  
455 localization error would decrease; at the same time, the resulting computational time will  
456 naturally increase. To investigate the effect of the projection image resolution, we took the  
457 original cone beam x-ray projection images with a resolution of  $1024 \times 768$  for patient 1 (Case 11)  
458 and down-sample them by a factor of 1, 2, 4, 8, 16, 32 on both dimensions of the projection  
459 images. The resulting images have the resolution of  $1024 \times 768$ ,  $512 \times 384$ ,  $256 \times 192$ ,  $128 \times 96$ ,  
460  $64 \times 48$  and  $32 \times 24$ , respectively. Figure 6 shows the average localization error on tangential and  
461 axial directions as well as computational time versus the downsampling factor. As expected, the  
462 average localization error increases monotonically as the downsampling factor increases.  
463 However, downsampling the projection image by a factor of 4 does not increase the localization

464 error noticeably. On the other hand, the computation time decreases monotonically as the  
 465 downsampling factor increases, but flattens out once it reaches 8. This supports the choice of a  
 466 resolution of  $256 \times 192$  (downsampling factor: 4) for the projection image used in this study,  
 467 because it achieves a reasonable balance between the localization accuracy and computational  
 468 time. Whether this observation holds true in general for clinical cases deserves further  
 469 investigation.  
 470



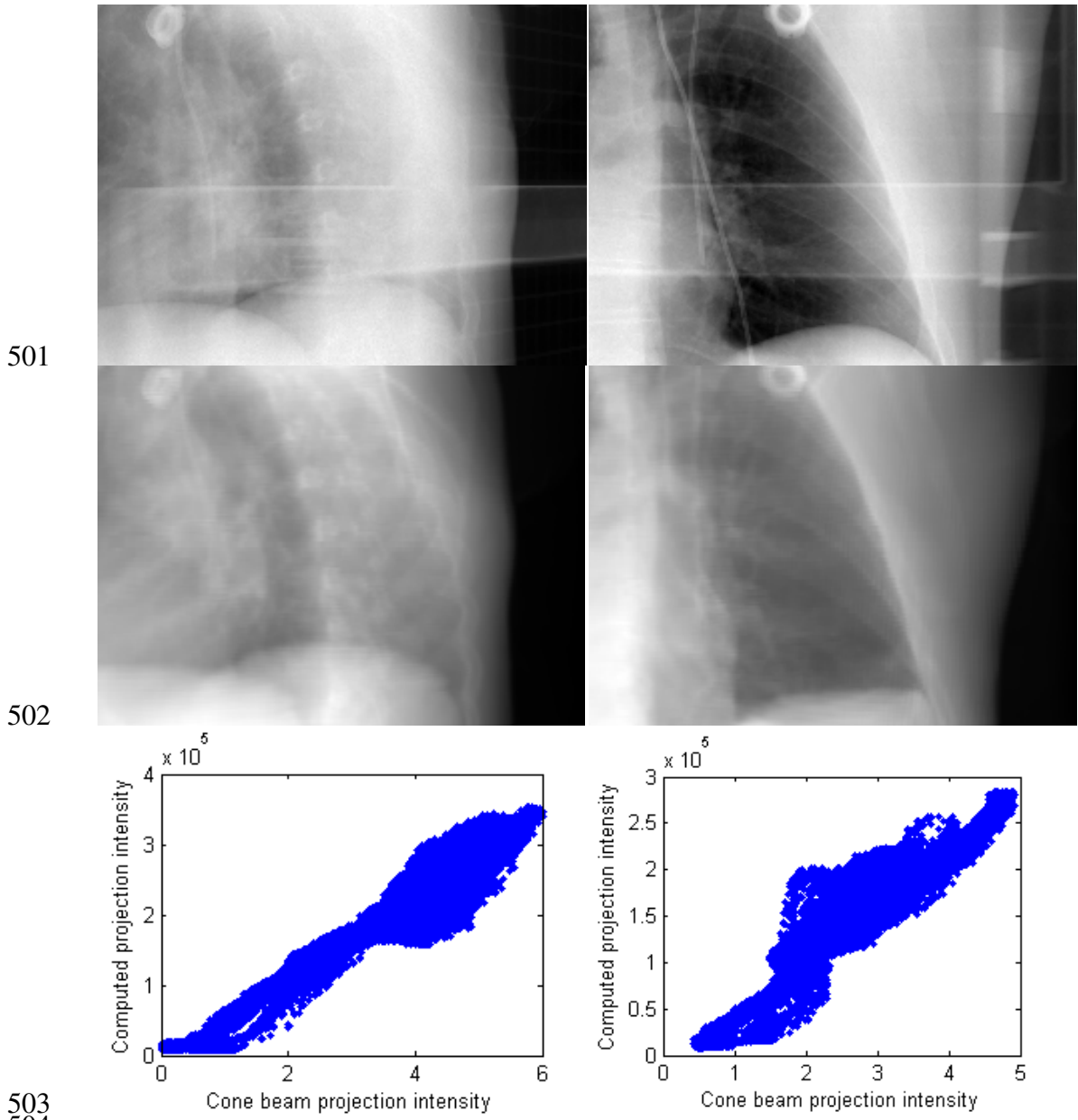
471 **Fig. 6.** The average localization error on tangential and axial directions as well as computational time  
 472 versus downsampling factor in one dimension of the x-ray imager for patient 1 (Case 11).  
 473  
 474

#### 475 **IV. Discussions**

476  
 477 We have developed an algorithm to localize 3D tumor positions in near real-time from a single x-  
 478 ray image. The algorithm was systematically tested on digital and physical respiratory phantoms  
 479 as well as lung cancer patients. For the digital phantom, the average 3D tumor localization error is  
 480 below 1 mm in the case of digital and physical phantoms. For the five lung cancer patients, the  
 481 average tumor localization error is below 2 mm in both the axial and tangential directions. By  
 482 utilizing the massive computing power of GPUs, we were able to derive 3D tumor locations from  
 483 one projection around 0.3 seconds on average. Successful applications of our algorithm in the  
 484 clinic could lead to accurate 3D tumor tracking from a single x-ray imager. Furthermore,  
 485 volumetric images can be reconstructed from a single x-ray projection image. This is potentially  
 486 useful for many clinical applications such as dose verification in lung cancer radiotherapy.  
 487

488 The tumor localization error in this work arises from two different processes: 1), the PCA lung  
 489 motion model; 2), the 2D to 3D deformable registration between the projection and the reference  
 490 image. In order to investigate how much each process contributes to the overall tumor  
 491 localization error, we utilized the ground truth of the 3D lung motion in the digital NCAT  
 492 phantom and solved for the optimal PCA coefficients by directly minimizing the mean square  
 493 error between the left and right sides in Eq. (1). This procedure bypassed the 2D to 3D  
 494 registration process, and thus gives the tumor localization error solely due to the PCA lung  
 495 motion model. In Case 1, this error is about 0.28 mm over all the projections. Assuming that the

496 above two processes are statistically independent, we readily obtain the error due to the 2D to 3D  
 497 registration process, which is about 0.75 mm. Therefore, the overall tumor localization error of  
 498 about 0.8 mm is mainly attributed to the 2D to 3D registration process. In comparison, the error  
 499 introduced by the PCA lung motion model is insignificant.  
 500



503  
 504  
 505 **Fig. 7.** Measured cone beam projections after preprocessing of the image intensities (logarithm transform  
 506 followed by reversion of the sign) (*top row*), computed projections of the reconstructed image (*middle*  
 507 *row*), and scatter plots between the intensities of the above two images (*bottom row*) for patient 1. Left  
 508 column corresponds to the EOE phase in Fig. 4 (arrow "a"); right column corresponds to the EOI phase in  
 509 Fig. 4 (arrow "b"). A linear model between the two image intensities is able to explain 94% and 91% of the  
 510 variance in the left and right subplot, respectively. Both linear models are significant ( $p < 0.001$ ).  
 511

512 In this work, we have assumed a linear relationship between the image intensities of the cone  
 513 beam projection and of the computed projection of the reconstructed image, in order to account  
 514 for the differences between the two image "modalities". One may wonder if such an assumption

515 is accurate in reality. After all, the x-ray energies as well as their spectra used for 4DCT and  
516 CBCT scans may well be different. There are several physical processes in reality (*e.g.*,  
517 scattering) which are not simulated in our computation of simulated x-ray projection. Figure 7  
518 shows the scatter plots between the image intensities of the preprocessed cone beam projection  
519 and of the computed projection of the reconstructed image at two different projection angles for  
520 patient 1, corresponding to the two projections shown in Fig. 5. It seems that a linear model is  
521 sufficient in both cases: more than 90% of the variance can be explained by a simple linear  
522 model. However, in the right subplot, because of more apparent interference from the treatment  
523 couch in the cone beam projection (which is absent in the computed projections), especially near  
524 the right edge, the linear model is less accurate than in the left subplot. This effect can be  
525 mitigated by pre-scanning the treatment couch and adding it to the reference image so that the  
526 couch will be also present in the computed projections.

527  
528 This work has focused on x-ray projections with rotational geometry. The same principle can be  
529 easily applied to those with fixed-angle geometry, such as fluoroscopy. The only difference is that  
530 the projection matrix will be constant for fixed-angle geometry instead of varying at each angle  
531 for the rotational geometry considered in this work.

532  
533 It is possible that during the course of the treatment patients may undergo anatomical changes on  
534 an inter-fractional basis, which could make the results worse if the lung motion model is built  
535 based on 4DCT acquired during patient simulation. In this case, a PCA lung motion model built  
536 from 4DCBCT during patient setup may overcome this difficulty. Another potential issue is when  
537 the tumor gets close to the heart. Then the tumor motion will be affected not only by breathing  
538 motion, but by heart motion too, which is not represented by the PCA motion model. This is a  
539 fundamental limitation of 4DCT, which is usually synchronized to respiration, not to cardiac  
540 motion.

541  
542 Although the results of five lung cancer patients confirmed the validity of our algorithm on a  
543 preliminary basis, a more comprehensive study on a larger patient population is warranted. It is  
544 worth mentioning that the accuracy of the tumor localization and image reconstruction is directly  
545 affected by the PCA lung motion model, which is in turn influenced by the quality of the training  
546 data (4DCT or 4DCBCT). Therefore, it is important to minimize the motion artifacts in the  
547 training data, *e.g.*, by optimizing the scanning protocol or coaching the patients to breathe  
548 regularly whenever possible. A reliable deformable registration algorithm, especially one which  
549 can accurately model large motion (*e.g.*, around the diaphragm), is also likely to help improve the  
550 accuracy the PCA lung motion model. In this work, since there were no fiducial markers  
551 implanted in the lung cancer patients, clinician marked tumor positions had to be used to evaluate  
552 the tumor localization results. The accuracy of the ground truth is thus limited due to noisy  
553 projection images as well as relatively poor soft-tissue contrast. For validation purposes, it would  
554 be beneficial to have patient data with implanted fiducial markers, from which better ground truth  
555 can be derived.

## 556 557 **V. Conclusions**

558  
559 In this work, we have presented an improved algorithm for 3D tumor localization from a single x-  
560 ray projection image by incorporating respiratory motion prediction. Through a comprehensive  
561 evaluation of our algorithm, we found the localization error to be less than 1 mm on average and  
562 around 2 mm at 95 percentile for both digital and physical phantoms, and within 2 mm on  
563 average and 4 mm at 95 percentile for five lung cancer patients on both axial and tangential  
564 directions. We also found that the localization accuracy is not affected by the breathing pattern,  
565 be it regular or irregular. The 3D localization can be achieved on a sub-second scale on GPU,  
566 requiring approximately 0.1 - 0.3 s for each x-ray projection.

567

568 **Acknowledgment**

569

570 This work is supported in part by Varian Master Research Agreement. We would like to thank Dr.  
 571 Paul Segars for providing the source code to generate NCAT phantom and NVIDIA for providing  
 572 GPU cards for this project. We would also like to thank the anonymous reviewers who gave  
 573 valuable comments and suggestions and helped improve this paper.

574

575 **Appendix**

576

577 In this appendix, we describe in detail the optimization of the cost function in Eq. (2) with respect  
 578 to  $\mathbf{w}, a, b$ . The optimization algorithm alternates between the following 2 steps:

$$579 \quad \text{step 1: } (a_{n+1}, b_{n+1})^T = (\mathbf{Y}^T \mathbf{Y})^{-1} \mathbf{Y}^T \mathbf{P} \mathbf{f}_n \quad (\text{A.1})$$

$$580 \quad \text{step 2: } \mathbf{w}_{n+1} = \mathbf{w}_n - \mu_n \cdot \frac{\partial J_n}{\partial \mathbf{w}_n} / \left\| \frac{\partial J_n}{\partial \mathbf{w}_n} \right\|_2 \quad (\text{A.2})$$

$$581 \quad \text{where, } \mathbf{Y} = [\mathbf{y}, \mathbf{1}], \text{ and } \frac{\partial J}{\partial \mathbf{w}} = \frac{\partial \mathbf{x}}{\partial \mathbf{w}} \cdot \frac{\partial \mathbf{f}}{\partial \mathbf{x}} \cdot \frac{\partial J}{\partial \mathbf{f}} = 2 \cdot \mathbf{U}^T \cdot \frac{\partial \mathbf{f}}{\partial \mathbf{x}} \cdot \mathbf{P}^T \cdot (\mathbf{P} \cdot \mathbf{f} - a \cdot \mathbf{y} - b \cdot \mathbf{1}).$$

582

583 It is easy to see that the above alternating algorithm consisting of steps 1 and 2 is guaranteed to  
 584 converge. In step 1, the update for a, b is the unique minimizer of the cost function with fixed  $\mathbf{w}$ .  
 585 Step 2 is a gradient descent method with variable  $\mathbf{w}$  and fixed a, b, where the step size  $\mu_n$  is  
 586 found by Armijo's rule<sup>22</sup> for line search. Therefore, the cost function always decreases at each  
 587 step. Note that the cost function is lower bounded by zero. The above alternating algorithm is  
 588 guaranteed to converge for all practical purposes. The parameters selected for line search are:  
 589 initial step size  $\mu_0 = 2$  and  $\alpha = 0.1, \beta = 0.5$  as defined by Armijo's rule. These values generally  
 590 lead to fast convergence and were used for all experiments in this study. The algorithm stops  
 591 whenever the step size for current iteration is sufficiently small (fixed at 0.1 in this paper). The  
 592 reason is that each PCA coefficients has been preconditioned so that their standard deviation is 10  
 593 in the training set; thus a step size of 0.1 can be considered sufficiently small and do not alter the  
 594 results significantly. The algorithm is also terminated when the maximum number of iterations is  
 595 reached (fixed at 10 in this paper). In the case of largest deformation from the reference image, it  
 596 takes around 8 or 9 iterations for the algorithm to 'converge', in the sense that the cost function  
 597 does not change much after that. Therefore, a maximum of 10 iterations should be sufficient to  
 598 get convergent results.

599 At each iteration, given the updated PCA coefficients in Eq. (A.2), the DVF is updated according  
 600 to Eq. (2) and the reconstructed image  $\mathbf{f}_{n+1}$  is obtained through trilinear interpolation.

601 Accordingly,  $\partial \mathbf{f} / \partial \mathbf{x}$  has to be consistent with the interpolation process in order to get the correct  
 602 gradient. Next, we derive the expression for  $\partial \mathbf{f} / \partial \mathbf{x}$ . Let  $\mathbf{f}_0(i, j, k)$  and  $\mathbf{f}(i, j, k)$  be the  
 603 reference image and reconstructed image at iteration  $n$  indexed by the integer set  
 604  $\{(i, j, k) | 1 \leq i \leq N_1, 1 \leq j \leq N_2, 1 \leq k \leq N_3\}$  within the bounding box of its volume, and  
 605  $\mathbf{x}_1(i, j, k), \mathbf{x}_2(i, j, k), \mathbf{x}_3(i, j, k)$  be the deformation vector fields corresponding to the three  
 606 canonical directions, namely, lateral, AP, and SI, respectively. They can be equivalently

607 reorganized into a vector whose length is the total number of voxels in the image. Then  
608  $\partial\mathbf{f}/\partial\mathbf{x} = [\partial\mathbf{f}/\partial\mathbf{x}_1; \partial\mathbf{f}/\partial\mathbf{x}_2; \partial\mathbf{f}/\partial\mathbf{x}_3]$ .  
609

610 Let's look at  $\partial\mathbf{f}/\partial\mathbf{x}_1$ . First notice that:

$$611 \quad \mathbf{f}(i, j, k) = \mathbf{f}_0(i + \mathbf{x}_1(i, j, k), j + \mathbf{x}_2(i, j, k), k + \mathbf{x}_3(i, j, k)) \quad (\text{A.3})$$

612 Then we have:

$$613 \quad \frac{\partial\mathbf{f}(i_1, j_1, k_1)}{\partial\mathbf{x}_1(i_2, j_2, k_2)} = \delta(i_1 - i_2)\delta(j_1 - j_2)\delta(k_1 - k_2) \cdot \frac{\partial\mathbf{f}(i_1, j_1, k_1)}{\partial\mathbf{x}_1(i_2, j_2, k_2)}. \quad (\text{A.4})$$

614 This means that the Jacobian matrix  $\partial\mathbf{f}/\partial\mathbf{x}_1$  is a diagonal matrix.

615

616 If the continuous patient geometry can be approximated by trilinear interpolation of the discrete  
617 volumetric image, then we have:

$$618 \quad \begin{aligned} \mathbf{f}(i, j, k) = & \mathbf{f}_0(l, m, n)(1 - z_1)(1 - z_2)(1 - z_3) + \mathbf{f}_0(l + 1, m, n)z_1(1 - z_2)(1 - z_3) \\ & + \mathbf{f}_0(l, m + 1, n)(1 - z_1)z_2(1 - z_3) + \mathbf{f}_0(l, m, n + 1)(1 - z_1)(1 - z_2)z_3 \\ & + \mathbf{f}_0(l + 1, m + 1, n)z_1z_2(1 - z_3) + \mathbf{f}_0(l + 1, m, n + 1)z_1(1 - z_2)z_3 \\ & + \mathbf{f}_0(l, m + 1, n + 1)(1 - z_1)z_2z_3 + \mathbf{f}_0(l + 1, m + 1, n + 1)z_1z_2z_3 \end{aligned} \quad (\text{A.5})$$

619 where,

620  $l = \lfloor i + \mathbf{x}_1(i, j, k) \rfloor, m = \lfloor j + \mathbf{x}_2(i, j, k) \rfloor, n = \lfloor k + \mathbf{x}_3(i, j, k) \rfloor$  are the integer parts of the DVF

621 and  $z_q = \{\mathbf{x}_q(i, j, k)\}, q = 1, 2, 3$  are the fractional parts of the DVF.

622

623 Notice that:

$$624 \quad \partial l / \partial \mathbf{x}_1 = \partial m / \partial \mathbf{x}_1 = \partial n / \partial \mathbf{x}_1 = 0 \quad (\text{A.6})$$

$$625 \quad \text{and } \partial z_1 / \partial \mathbf{x}_1 = 1, \quad \partial z_2 / \partial \mathbf{x}_1 = \partial z_3 / \partial \mathbf{x}_1 = 0 \quad (\text{A.7})$$

626 where, for simplicity, we have omitted the index  $(i, j, k)$  for  $\mathbf{x}_1$ .

627

628 From Eq. (A.5)-(A.7), we immediately get:

$$629 \quad \begin{aligned} \partial\mathbf{f}(i, j, k) / \partial\mathbf{x}_1(i, j, k) = & [\mathbf{f}_0(l + 1, m, n) - \mathbf{f}_0(l, m, n)](1 - z_2)(1 - z_3) \\ & + [\mathbf{f}_0(l + 1, m + 1, n) - \mathbf{f}_0(l, m + 1, n)]z_2(1 - z_3) \\ & + [\mathbf{f}_0(l + 1, m, n + 1) - \mathbf{f}_0(l, m, n + 1)](1 - z_2)z_3 \\ & + [\mathbf{f}_0(l + 1, m + 1, n + 1) - \mathbf{f}_0(l, m + 1, n + 1)]z_2z_3 \end{aligned} \quad (\text{A.8})$$

630

631 Similar expressions can be derived for  $\partial\mathbf{f}/\partial\mathbf{x}_2$  and  $\partial\mathbf{f}/\partial\mathbf{x}_3$ .

632

633 A few comments are appropriate at this point. Equation (A.8) is the exact derivative given the  
634 continuous patient geometry obtained from trilinear interpolation in Eq. (A.5). Of course, any  
635 reasonable kind of interpolation can be used here, *e.g.*, tricubic interpolation. Then the Jacobian  
636 matrix  $\partial\mathbf{f}/\partial\mathbf{x}_1$  does not have a nice diagonal form anymore, but may be block diagonal. It is clear  
637 from Eq. (A.8) that  $\partial\mathbf{f}/\partial\mathbf{x}$  is a linear combination of the spatial gradients of the reference image  
638 evaluated at the neighboring eight grid points, weighted by the appropriate fractional parts of the  
639 DVF. At this stage,  $\partial\mathbf{f}/\partial\mathbf{x}$  contains only local information at the level of individual voxels. It is

640 the eigenvectors that effectively combine all the local information into global information and  
641 lead to correct update for the PCA coefficients.

642

643 For trilinear interpolation,  $\mathbf{f}$  is continuous but not differentiable at the boundaries of the voxel  
644 grids, so that Eq. (A.6)-(A.7) do not hold in this situation. However, this happens with a  
645 probability of 0. If it does happen, Eq. (A.8) simply computes the right-side derivative and will  
646 not create numerical instability. What's more, even if it happens that the DVFs are integers at a  
647 few voxels, the pooling effects of the eigenvectors will almost eliminates its influence by a vast  
648 majority of other voxels.

649

650

651 **References**

652

- 653 1. P. J. Keall, G. S. Mageras, J. M. Balter, R. S. Emery, K. M. Forster, S. B. Jiang, J.  
654 M. Kapatoes, D. A. Low, M. J. Murphy, B. R. Murray, C. R. Ramsey, M. B. Van  
655 Herk, S. S. Vedam, J. W. Wong and E. Yorke, "The management of respiratory  
656 motion in radiation oncology report of AAPM Task Group 76," *Med Phys* **33**,  
657 3874-3900 (2006).
- 658 2. T. Harada, H. Shirato, S. Ogura, S. Oizumi, K. Yamazaki, S. Shimizu, R.  
659 Onimaru, K. Miyasaka, M. Nishimura and H. Dosaka-Akita, "Real-time tumor-  
660 tracking radiation therapy for lung carcinoma by the aid of insertion of a gold  
661 marker using bronchofiberscopy," *Cancer* **95**, 1720-1727. (2002).
- 662 3. F. Laurent, V. Latrabe, B. Vergier, M. Montaudon, J. M. Vernejoux and J.  
663 Dubrez, "CT-guided transthoracic needle biopsy of pulmonary nodules smaller  
664 than 20 mm: results with an automated 20-gauge coaxial cutting needle," *Clin*  
665 *Radiol* **55**, 281-287 (2000).
- 666 4. J. D. Hoisak, K. E. Sixel, R. Tirona, P. C. Cheung and J. P. Pignol, "Correlation  
667 of lung tumor motion with external surrogate indicators of respiration," *Int J*  
668 *Radiat Oncol Biol Phys* **60**, 1298-1306 (2004).
- 669 5. Y. Tsunashima, T. Sakae, Y. Shioyama, K. Kagei, T. Terunuma, A. Nohtomi and  
670 Y. Akine, "Correlation between the respiratory waveform measured using a  
671 respiratory sensor and 3D tumor motion in gated radiotherapy," *Int J Radiat Oncol*  
672 *Biol Phys* **60**, 951-958 (2004).
- 673 6. Y. Cui, J. G. Dy, G. C. Sharp, B. Alexander and S. B. Jiang, "Multiple template-  
674 based fluoroscopic tracking of lung tumor mass without implanted fiducial  
675 markers," *Phys Med Biol* **52**, 6229-6242 (2007).
- 676 7. Q. Xu, R. J. Hamilton, R. A. Schowengerdt, B. Alexander and S. B. Jiang, "Lung  
677 Tumor Tracking in Fluoroscopic Video Based on Optical Flow," *Medical Physics*  
678 **35**, 5351-5359 (2008).
- 679 8. T. Lin, L. I. Cervino, X. Tang, N. Vasconcelos and S. B. Jiang, "Fluoroscopic  
680 tumor tracking for image-guided lung cancer radiotherapy," *Phys Med Biol* **54**,  
681 981-992 (2009).
- 682 9. J. H. Lewis, R. Li, W. T. Watkins, J. D. Lawson, W. P. Segars, L. I. Cervino, W.  
683 Y. Song and S. B. Jiang, "Markerless lung tumor tracking and trajectory  
684 reconstruction using rotational cone-beam projections: a feasibility study," *Phys*  
685 *Med Biol* **55**, 2505-2522 (2010).
- 686 10. R. Zeng, J. A. Fessler and J. M. Balter, "Estimating 3-D respiratory motion from  
687 orbiting views by tomographic image registration," *IEEE Trans Med Imaging* **26**,  
688 153-163 (2007).
- 689 11. Q. Zhang, A. Pevsner, A. Hertanto, Y. C. Hu, K. E. Rosenzweig, C. C. Ling and  
690 G. S. Mageras, "A patient-specific respiratory model of anatomical motion for  
691 radiation treatment planning," *Med Phys* **34**, 4772-4781 (2007).
- 692 12. D. A. Low, P. J. Parikh, W. Lu, J. F. Dempsey, S. H. Wahab, J. P. Hubenschmidt,  
693 M. M. Nystrom, M. Handoko and J. D. Bradley, "Novel breathing motion model  
694 for radiotherapy," *Int J Radiat Oncol Biol Phys* **63**, 921-929 (2005).
- 695 13. R. Li, J. H. Lewis, X. Jia, T. Zhao, W. Liu, S. Wuenschel, J. Lamb, D. Yang, D.  
696 A. Low and S. B. Jiang, "A PCA-based lung motion model," *Phys Med Biol*  
697 *submitted* (2010).

- 698 14. R. Li, X. Jia, J. H. Lewis, X. Gu, M. Folkerts, C. Men and S. B. Jiang, "Real-time  
699 volumetric image reconstruction and 3D tumor localization based on a single x-  
700 ray projection image for lung cancer radiotherapy," *Med. Phys.* **37**, 2822-2826  
701 (2010).
- 702 15. M. J. Murphy, J. Jalden and M. Isaksson, presented at the Proc. 16th Int. Conf. on  
703 Computer Assisted Radiology (CARS 2002), Paris, France, 2002 (unpublished).
- 704 16. G. C. Sharp, S. B. Jiang, S. Shimizu and H. Shirato, "Prediction of respiratory  
705 tumour motion for real-time image-guided radiotherapy," *Phys Med Biol* **49**, 425-  
706 440 (2004).
- 707 17. D. Ruan, J. A. Fessler and J. M. Balter, "Real-time prediction of respiratory  
708 motion based on local regression methods," *Phys Med Biol* **52**, 7137-7152 (2007).
- 709 18. M. Chen, W. Lu, Q. Chen, K. J. Ruchala and G. H. Olivera, "A simple fixed-point  
710 approach to invert a deformation field," *Med Phys* **35**, 81-88 (2008).
- 711 19. X. Gu, H. Pan, Y. Liang, R. Castillo, D. Yang, D. Choi, E. Castillo, A. Majumdar,  
712 T. Guerrero and S. B. Jiang, "Implementation and evaluation of various demons  
713 deformable image registration algorithms on a GPU," *Phys Med Biol* **55**, 207-219  
714 (2010).
- 715 20. W. P. Segars, "Development and application of the new dynamic NURBS-based  
716 cardiac-torso (NCAT) phantom," Ph.D. Dissertation (2001).
- 717 21. R. L. Siddon, "Fast calculation of the exact radiological path for a three-  
718 dimensional CT array," *Medical Physics* **12**, 252-255 (1985).
- 719 22. M. S. Bazaraa, H. D. Sherali and C. M. Shetty, *Nonlinear Programming: Theory*  
720 *and Algorithms*. (Hoboken: A John Wiley & Sons, 2006).
- 721  
722

---

<sup>a</sup> Email: sbjiang@ucsd.edu